The Astrophysical Journal, 780:103 (8pp), 2014 January 1 doi:10.1088/0004-637X/780/1/103

EVIDENCE FOR TWO SEPARATE HELIOSPHERIC CURRENT SHEETS OF CYLINDRICAL SHAPE DURING MID-2012

Y.-M. Wang[1], P. R. Young[2], and K. Muglach[3,4]
[1] Space Science Division, Naval Research Laboratory, Washington, DC 20375, USA; yi.wang@nrl.navy.mil
[2] College of Science, George Mason University, Fairfax, VA 22030, USA; pyoung@ssd5.nrl.navy.mil
[3] Code 674, NASA Goddard Space Flight Center, Greenbelt, MD 20771, USA; karin.muglach@nasa.gov
Received 2013 September 24; accepted 2013 November 20; published 2013 December 13

ABSTRACT

During the reversal of the Sun's polar fields at sunspot maximum, outward extrapolations of magnetograph measurements often predict the presence of two or more current sheets extending into the interplanetary medium, instead of the single heliospheric current sheet (HCS) that forms the basis of the standard "ballerina skirt" picture. By comparing potential-field source-surface models of the coronal streamer belt with white-light coronagraph observations, we deduce that the HCS was split into two distinct structures with circular cross sections during mid-2012. These cylindrical current sheets were centered near the heliographic equator and separated in longitude by roughly 180°; a corresponding four-sector polarity pattern was observed at Earth. Each cylinder enclosed a negative-polarity coronal hole that was identifiable in extreme ultraviolet images and gave rise to a high-speed stream. The two current sheet systems are shown to be a result of the dominance of the Sun's nonaxisymmetric quadrupole component, as the axial dipole field was undergoing its reversal during solar cycle 24.

Key words: interplanetary medium – solar wind – Sun: activity – Sun: corona – Sun: heliosphere – Sun: magnetic fields

Online-only material: color figures

1. INTRODUCTION

As reviewed by Smith (2001), the heliospheric current sheet (HCS) is generally thought of as a single, warped structure that extends outward from the corona and separates the Sun's inward- and outward-directed magnetic field. This picture is supported by potential-field source-surface (PFSS) and magnetohydrodynamical extrapolations of photospheric magnetograms (see, e.g., Hoeksema et al. 1982; Riley et al. 2002). Such extrapolations have been remarkably successful in reproducing the observed variation of the interplanetary sector structure at Earth (as illustrated by Figure 8 in Wang et al. 2009), suggesting that they provide a reasonable approximation to the large-scale topology of the HCS. In these models, only one neutral/current sheet is normally present because of the dominance of the Sun's dipole component at heliocentric distances $r \gtrsim 2\,R_\odot$; higher-order magnetic multipoles act to warp the HCS without causing it to split apart (see, e.g., Petrie & Haislmaier 2013). However, during a brief interval coinciding with the reversal of the polar fields, the total dipole moment may become so weak that higher-order multipoles dominate, giving rise to two or more separate current sheets.

Employing PFSS extrapolations and white-light coronagraph observations, we here show that the HCS split into two cylindrical current sheets in mid-2012, during the maximum phase of the ongoing solar cycle 24. The white-light data were recorded by the Large Angle and Spectrometric Coronagraph (LASCO) on the *Solar and Heliospheric Observatory* (*SOHO*) and by the COR2 coronagraphs on *STEREO A*/*B*.

2. METHOD

In order to identify the location of the HCS in coronal streamer maps, it is important to distinguish between plasma sheets that contain polarity reversals and those that do not. For this purpose, we apply a PFSS extrapolation to photospheric field measurements for the given Carrington rotation (CR), and determine the locations and polarities of all open field regions (coronal holes) at the solar surface. The hole boundaries are mapped from $r = R_\odot$ to the source surface $r = R_{ss} = 2.5\,R_\odot$, where the magnetic field is constrained to be purely radial and hence "open." There, the boundary lines that separate opposite-polarity holes define the angular location of the HCS and its associated helmet-streamer plasma sheet. The rest of the boundary lines separate open flux originating from like-polarity holes; these separatrices define the locations of the "pseudostreamer" plasma sheets that contribute to the white-light streamer patterns in the outer corona but are not directly related to the HCS (see Wang et al. 2007).

In order to allow direct comparison with the observed streamer structures, we employ the formulae of Billings (1966) to calculate the sky-plane brightness patterns resulting from Thomson scattering by the radially oriented plasma sheets, which are taken to be 4° wide. As in Wang et al. (2007), the electron density is assumed to fall off as $r^{-2.5}$ and to be three times lower in the pseudostreamer than in the helmet-streamer plasma sheet(s).

For the photospheric field data, we employ Carrington maps from the Mount Wilson Observatory (MWO). As in Wang & Sheeley (1995), the magnetograph measurements are deprojected by dividing by cos L (where L denotes heliographic latitude) and corrected for the saturation of the Fe I 525.0 nm line profile by multiplying by $(4.5–2.5 \sin^2 L)$. For the white-light coronagraph data, we use east- and west-limb synoptic maps constructed from *SOHO* LASCO C3 images by N. B. Rich[5] and from *STEREO* COR2A/B images by A. F. R. Thernisien.[6] The

[4] Also at ARTEP, Inc., Ellicott City, MD 21042, USA.

[5] See http://lasco-www.nrl.navy.mil/carr_maps/.
[6] See http://secchi.nrl.navy.mil/synomaps/.

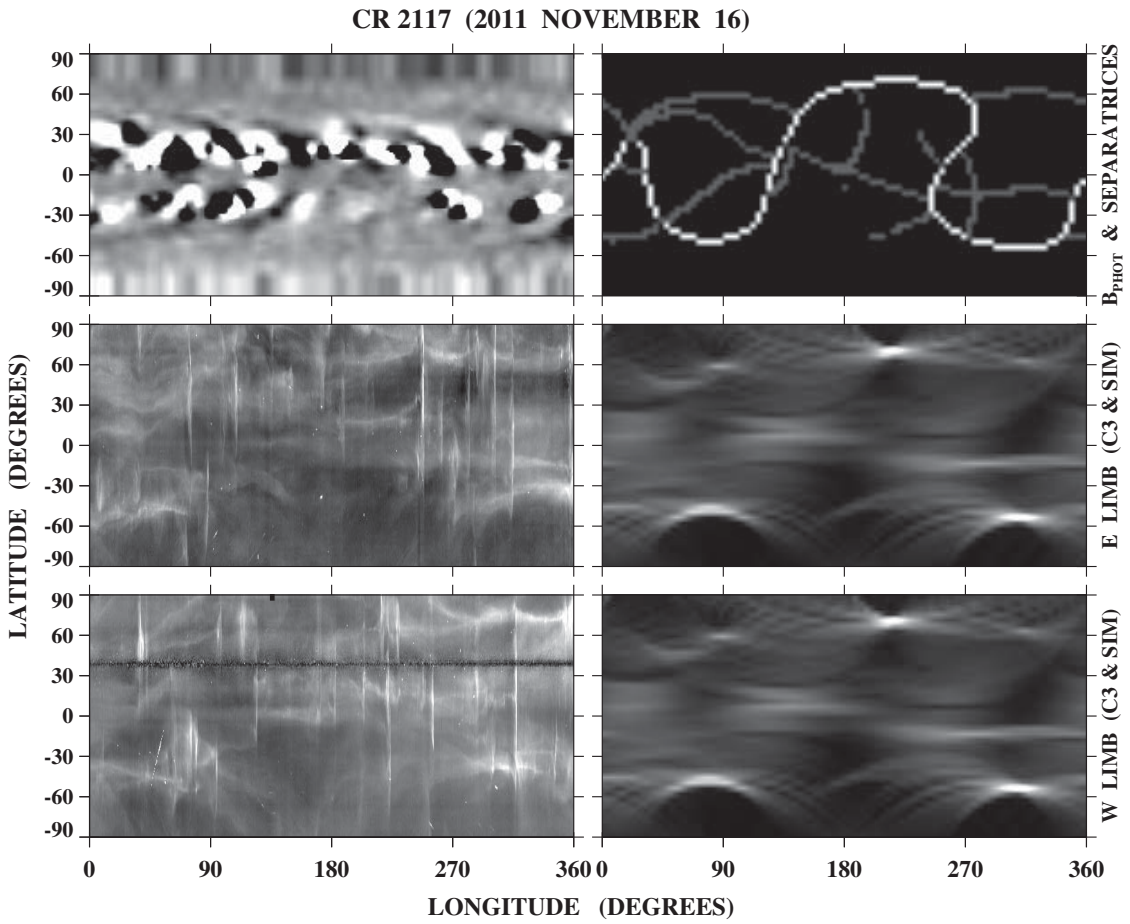

Figure 1. Observed and simulated coronal streamer structures during CR 2117 (starting date 2011 November 16). Top left: MWO map of the photospheric field, saturated at $B_r < -10$ G (black) and $B_r > +10$ G (white). Top right: boundaries between open field regions at $r = R_{ss} = 2.5\,R_\odot$, derived by applying a PFSS extrapolation to the photospheric map. White pixels represent the source-surface neutral line (or predicted position of the HCS and helmet-streamer plasma sheet); gray pixels mark the boundaries between coronal holes of the same polarity (or predicted locations of pseudostreamer plasma sheets). Middle left: white-light streamer structures observed above the east limb at 10 $R_\odot$ with the *SOHO*/LASCO C3 coronagraph. Middle right: simulated brightness patterns above the east limb, produced by Thomson scattering of photospheric radiation from the helmet-streamer and pseudostreamer plasma sheets. Bottom left: west-limb streamer structures observed at 10 $R_\odot$ by LASCO C3. Bottom right: simulated west-limb streamer structures. Vertical streaks in the LASCO maps represent coronal mass ejections (CMEs). Even though they are derived from the same photospheric field map, the simulated east- and west-limb streamer patterns may differ from each other if the solar rotation axis is tilted with respect to the observer (see Wang et al. 2000); during CR 2117, however, the B angle is close to zero, so that the maps in the middle and bottom right panels are practically indistinguishable.

maps were created by extracting strips of data centered at 10 $R_\odot$ from successive images and arranging them in time-reversed order.

As an example, Figure 1 displays the MWO photospheric field, hole boundaries at the source surface, and observed and simulated streamer patterns during CR 2117 (starting date 2011 November 16), when northern hemisphere sunspot activity was near its peak. In the source-surface map, white pixels represent the neutral line (i.e., the boundaries between coronal holes of opposite polarity), while gray pixels mark the predicted pseudostreamer locations (i.e., the boundaries between holes of the same polarity); the helmet-streamer and pseudostreamer plasma sheets are assumed to extend radially outward from these separatrices. The white-light data are from LASCO C3, and are shown separately for the east limb (middle left panel) and west limb (bottom left panel); the west-limb observations were taken ~13.6 days after those at the east limb. The corresponding simulations are displayed at the right. The brightest structures in the observed and simulated streamer maps occur at those locations where the plasma sheets are viewed edge-on in the sky plane, which in turn correspond to the places where the boundary lines in the source-surface map run horizontally. As the plasma sheets rotate into and out of the sky plane, moving from higher to lower apparent latitudes and upward again, they trace out arclike patterns, with the bottom of the arc representing the actual latitude of the streamer or pseudostreamer.

Despite the complex appearance of the streamer belt, with its extensive network of pseudostreamer plasma sheets, we conclude from Figure 1 that only one source-surface neutral line/HCS was present during CR 2117. The HCS undergoes two northward and two southward excursions, indicating that the photospheric field has a significant ($l = 2, |m| = 2$) quadrupole component in addition to the still dominant dipole. As may be seen from the *STEREO* Fe XII 19.5 nm map in Figure 2, the large northward excursion is associated with an equatorward lobe of the south polar hole, which still has its pre-reversal (positive) polarity; a corresponding negative-polarity remnant of the north polar hole is present at Carrington longitude $\phi \sim 90^\circ$.

3. BIFURCATION OF THE HCS DURING 2012

Figures 3 and 4 display the observed and simulated streamer patterns for CR 2123 (starting date 2012 April 28) and

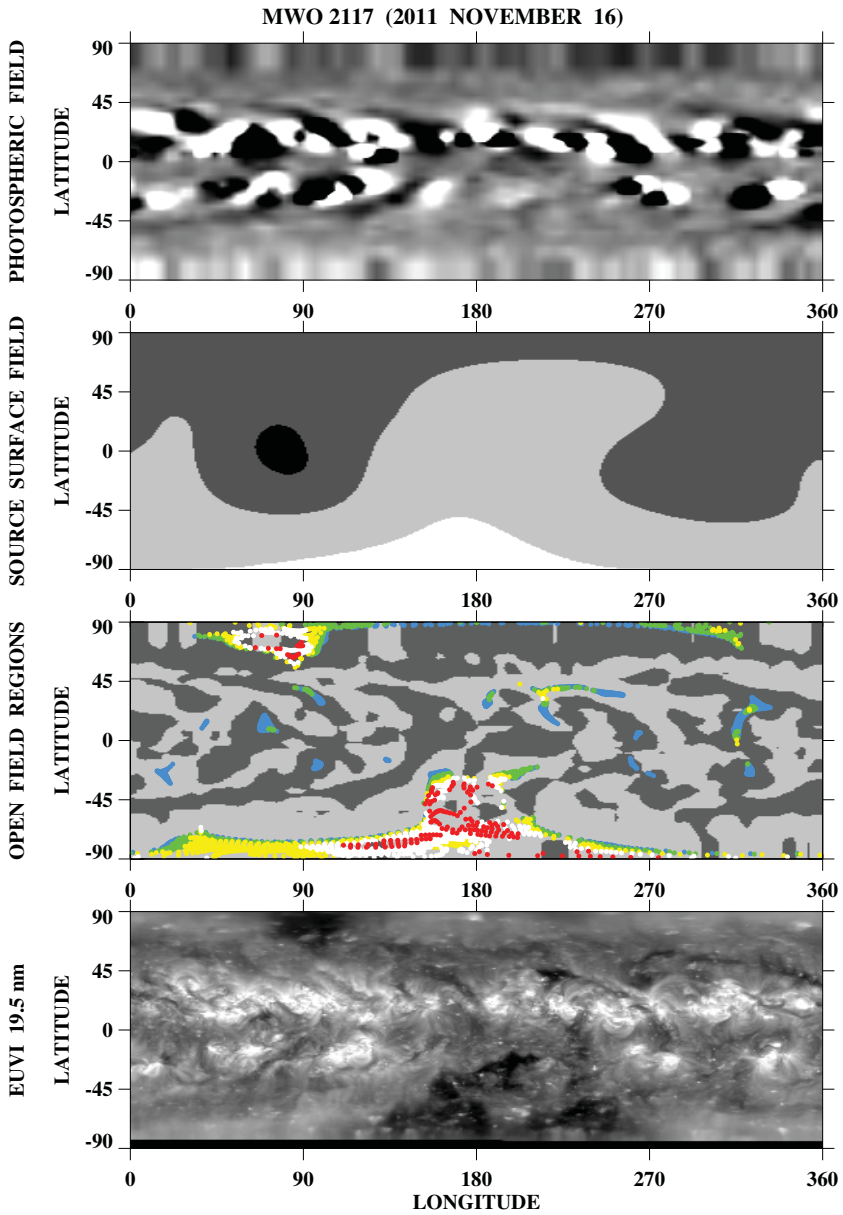

Figure 2. Latitude–longitude maps showing the large-scale field and distribution of coronal holes during CR 2117. Top panel: MWO photospheric field, with gray scale contours ranging from black ($B_r < -10$ G) to white ($B_r > +10$ G). Note that the polar fields still have their old-cycle polarity (negative in the north, positive in the south). Second panel: source-surface field $B_{ss} = B_r(R_{ss}, L, \phi)$. Black: $B_{ss} < -0.15$ G; dark gray: -0.15 G $< B_{ss} < 0$ G; light gray: 0 G $< B_{ss} < +0.15$ G; white: $B_{ss} > +0.15$ G. Third panel: PFSS-derived coronal holes. Colored dots represent footpoints of open field lines and are coded according to the associated expansion factors or asymptotic wind speeds. Blue: $v < 450$ km s^{-1} ($f_{ss} > 24$); green: $v = 450$–550 km s^{-1} ($12 < f_{ss} < 24$); yellow: $v = 550$–650 km s^{-1} ($7 < f_{ss} < 12$); white: $v = 650$–750 km s^{-1} ($4 < f_{ss} < 7$); red: $v > 750$ km s^{-1} ($f_{ss} < 4$). The polarity of the underlying photospheric field is indicated by dark gray (if $B_r < 0$) or light gray (if $B_r > 0$). Bottom panel: distribution of Fe XII 19.5 nm emission recorded by the Extreme Ultraviolet Imager (EUVI) on *STEREO B* between November 8 and December 5. Dark areas represent coronal holes or filament channels.

(A color version of this figure is available in the online journal.)

CR 2124 (starting date 2012 May 25), respectively. During both rotations, two roughly circular neutral lines, centered near the equator and separated by ~180° in longitude, are present at the source surface. The outward extension of each neutral line has the form of a cylindrical current/plasma sheet, which gives rise to a pair of arclike features at its northern- and southernmost latitudes, where the sheet is oriented edge-on at the solar limb. As is apparent from the simulated white-light maps in Figures 3 and 4, each pair of arcs is positioned around a single longitude, in contrast to the case of a single warped HCS, whose latitudinal maxima and associated arclike brightenings are generally widely spaced in longitude.

Allowing for perturbations due to transient events, we find reasonable agreement between the observed and simulated streamer patterns in Figures 3 and 4. As indicated by the white arrows, each of the arclike features produced by the two cylindrical plasma/current sheets can be identified in the LASCO and COR2 synoptic maps for CR 2123 and 2124. At the same time, it is evident that a substantial fraction of the white-light coronal structure around sunspot maximum is contributed by the extensive network of pseudostreamer plasma sheets, rather than being associated with the HCS.

Figure 5 shows Carrington-format maps of the photospheric and source-surface fields, PFSS-derived open field regions, and

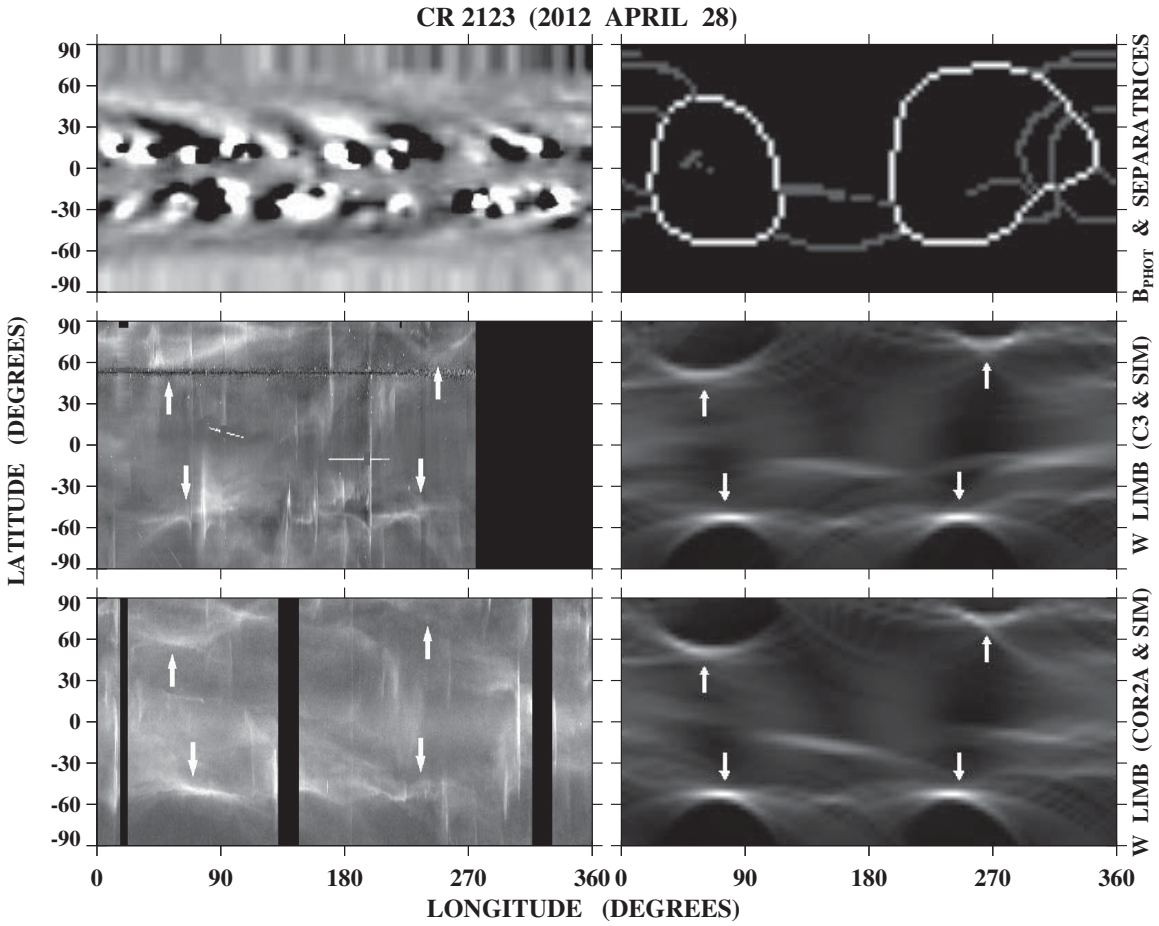

Figure 3. Observed and simulated coronal streamer structures during CR 2123 (starting date 2012 April 28). Top left: MWO photospheric field. Top right: boundaries between coronal holes at the source surface, with white pixels marking the two circular neutral lines and gray pixels indicating the positions of pseudostreamer plasma sheets. Middle left: white-light streamer patterns at 10 $R_\odot$, recorded above the west limb by *SOHO*/LASCO C3 between May 4 and June 1. Middle right: simulated streamer structures above the west limb (using the *B* angle appropriate for *SOHO*). Bottom left: white-light streamer patterns at 10 $R_\odot$, recorded above the west limb by *STEREO*/COR2A between May 13 and June 10. Bottom right: simulated streamer structures above the west limb (using the *B* angle appropriate for *STEREO A*). White arrows in the observed and simulated streamer maps point to the arclike features produced by Thomson scattering from the horizontal (edge-on) portions of the two cylindrical current/plasma sheets. Vertical streaks in the coronagraph observations represent CMEs.

extreme ultraviolet (EUV) coronal holes for CR 2124. Each of the two circular neutral lines at the source surface is centered above a negative-polarity hole, which is clearly seen in both the PFSS calculation (third panel) and the Fe XII 19.5 nm map (bottom panel). These coronal holes (circled) are surrounded by holes of the opposite polarity, so that the negative-polarity open flux is confined to two islands immersed in a sea of positive-polarity open flux. Although the north polar field is still weakly negative at this time, the old-cycle polar hole has disappeared and the polar cap is bordered by longitudinally extended holes of positive polarity; accordingly, the high-latitude source-surface/interplanetary field has now changed from negative to positive. In the southern hemisphere, by contrast, a large remnant of the old-cycle polar hole is still present, so that the source-surface field has the same (positive) sign above the south pole as above the north pole. The time lag between the disappearance of the north and south polar holes reflects the lag in sunspot activity between the two hemispheres, with the northern hemisphere having been far more active during the rising phase of the cycle (see, e.g., Robbrecht & Wang 2012; Shiota et al. 2012; Svalgaard & Kamide 2013).

4. MAGNETIC MULTIPOLE ANALYSIS

The unusual topology of the HCS during mid-2012 and its relationship to the polar field reversal can also be understood by decomposing the Sun's large-scale field into its spherical harmonic components. The axial ($l = 1, m = 0$) and equatorial ($l = 1, |m| = 1$) components of the total dipole strength $D_{\rm tot} = (D_{\rm ax}^2 + D_{\rm eq}^2)^{1/2}$ are related to the photospheric flux distribution $B_r(R_\odot, L, \phi)$ by

$$D_{\rm ax} = \frac{3}{4\pi} \int B_r(R_\odot, L, \phi) \sin L d\Omega, \quad (1)$$

$$D_{\rm eq} = \left(H_1^2 + H_2^2\right)^{1/2}, \quad (2)$$

$$H_1 = \frac{3}{4\pi} \int B_r(R_\odot, L, \phi) \cos L \cos \phi d\Omega, \quad (3)$$

$$H_2 = \frac{3}{4\pi} \int B_r(R_\odot, L, \phi) \cos L \sin \phi d\Omega, \quad (4)$$

where the integrals are taken over all solid angles Ω. To measure the average strength of a given multipole or spherical harmonic

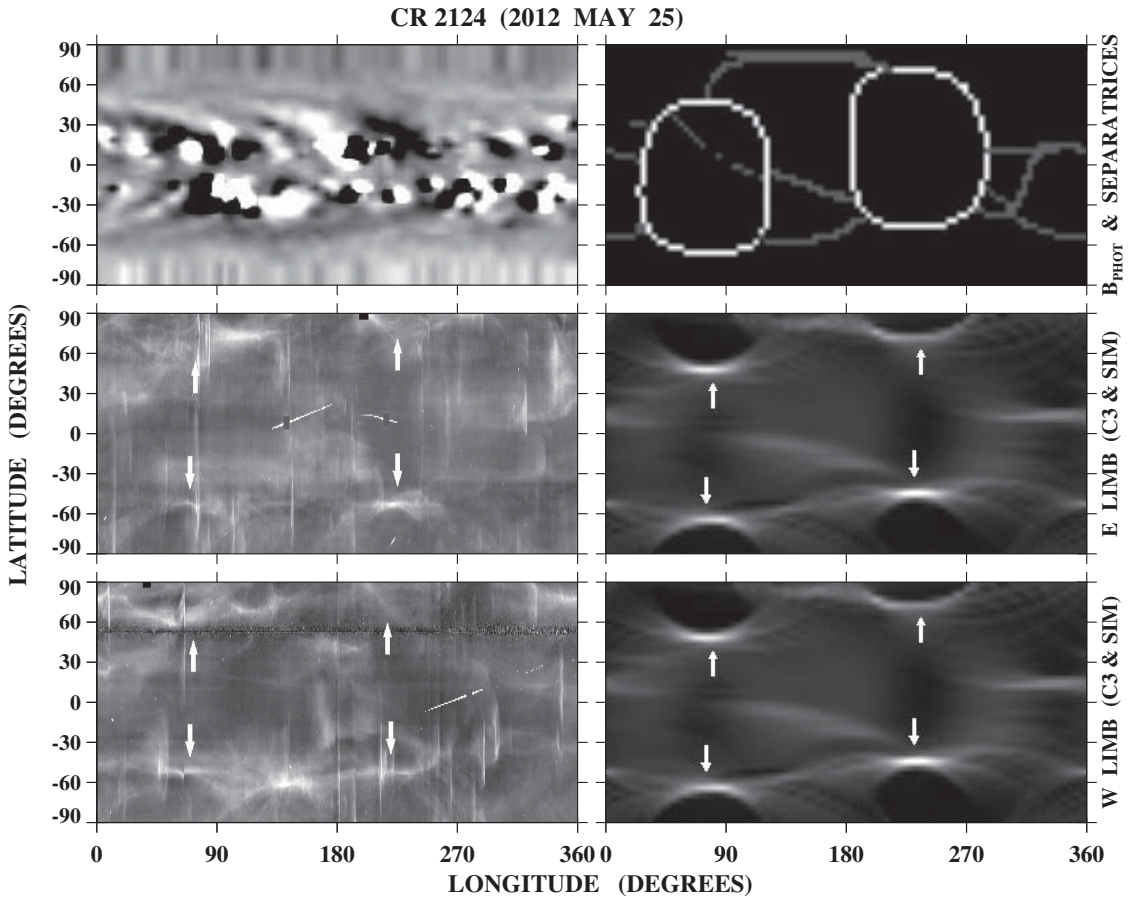

Figure 4. Observed and simulated coronal streamer structures during CR 2124 (starting date 2012 May 25). Top left: MWO photospheric field. Top right: boundaries between coronal holes at the source surface, with white pixels marking the two circular neutral lines and gray pixels indicating the positions of pseudostreamer plasma sheets. Middle left: white-light streamer patterns at 10 $R_\odot$, recorded above the east limb by LASCO C3 between May 18 and June 14. Middle right: simulated streamer structures above the east limb. Bottom left: white-light streamer patterns at 10 $R_\odot$, recorded above the west limb by LASCO C3 between June 1 and June 28. Bottom right: simulated streamer structures above the west limb. Again, white arrows indicate the arc-shaped brightenings associated with the poleward sides of the two cylindrical current/plasma sheets.

component at $r = R_{ss}$, we write the source-surface field in the general form

$$B_r(R_{ss}, L, \phi) = \sum_{l=1}^{\infty} b_l(R_{ss}, L, \phi) = \sum_{l=1}^{\infty} \sum_{m=-l}^{l} b'_{lm}(R_{ss}, L, \phi)$$
$$= \sum_{l=1}^{\infty} \sum_{m=0}^{l} b_{lm}(R_{ss}, L, \phi) \quad (5)$$

(b_{lm} is given explicitly in terms of the spherical harmonic function Y_{lm} and its complex conjugate by Equations (1) and (2) in Wang & Sheeley 1988). We then define

$$\langle b_l \rangle \equiv \frac{1}{4\pi} \int |b_l(R_{ss}, L, \phi)| d\Omega, \quad (6)$$

$$\langle b_{lm} \rangle \equiv \frac{1}{4\pi} \int |b_{lm}(R_{ss}, L, \phi)| d\Omega. \quad (7)$$

Figure 6(a) shows the time variation of D_{tot}, D_{ax}, and D_{eq} during 2011–2012, as derived from the MWO photospheric field measurements for CR 2105–2132 (the curves have been smoothed by taking three-rotation running means). The axial dipole component approaches zero in the middle of 2012, while the equatorial dipole strength decreases to small but finite values. In Figure 6(b), we plot $\langle b_1 \rangle$, $\langle b_2 \rangle$, $\langle b_{22} \rangle$, and $\langle b_{20} \rangle$ for the same time interval. The total quadrupole strength at the source surface, $\langle b_2 \rangle$, reaches a peak in mid-2012, when it greatly exceeds the total dipole strength $\langle b_1 \rangle$. The quadrupole is in turn dominated by its sectoral component $\langle b_{22} \rangle$, whereas its axisymmetric component $\langle b_{20} \rangle$ is of order $\langle b_1 \rangle$. We remark that very similar results are obtained using magnetograph data from the National Solar Observatory (NSO/Kitt Peak) and from the Wilcox Solar Observatory (WSO).

It is now evident that the bifurcation of the HCS during mid-2012 was due to the dominance of the (2, 2) quadrupole component at the source surface. The nonaxisymmetric quadrupole increased in strength just as the axial dipole was undergoing its polarity reversal; another necessary condition for the splitting into two or more current sheets is that the equatorial dipole remain weak, as was indeed the case. Furthermore, the dominance of the axisymmetric quadrupole over the axial dipole component ($\langle b_{20} \rangle \gg \langle b_{10} \rangle$) explains why the source-surface field had the same sign at both poles (see the second panel in Figure 5).

Figure 7 displays the PFSS-derived coronal fieldline configuration during CR 2124, as viewed from above the north and south poles. It is again apparent that the large-scale magnetic field, with its four regularly spaced loop arcades, has an almost purely (2, 2) quadrupole nature at this time. Although some negative-polarity photospheric flux is still present at the north

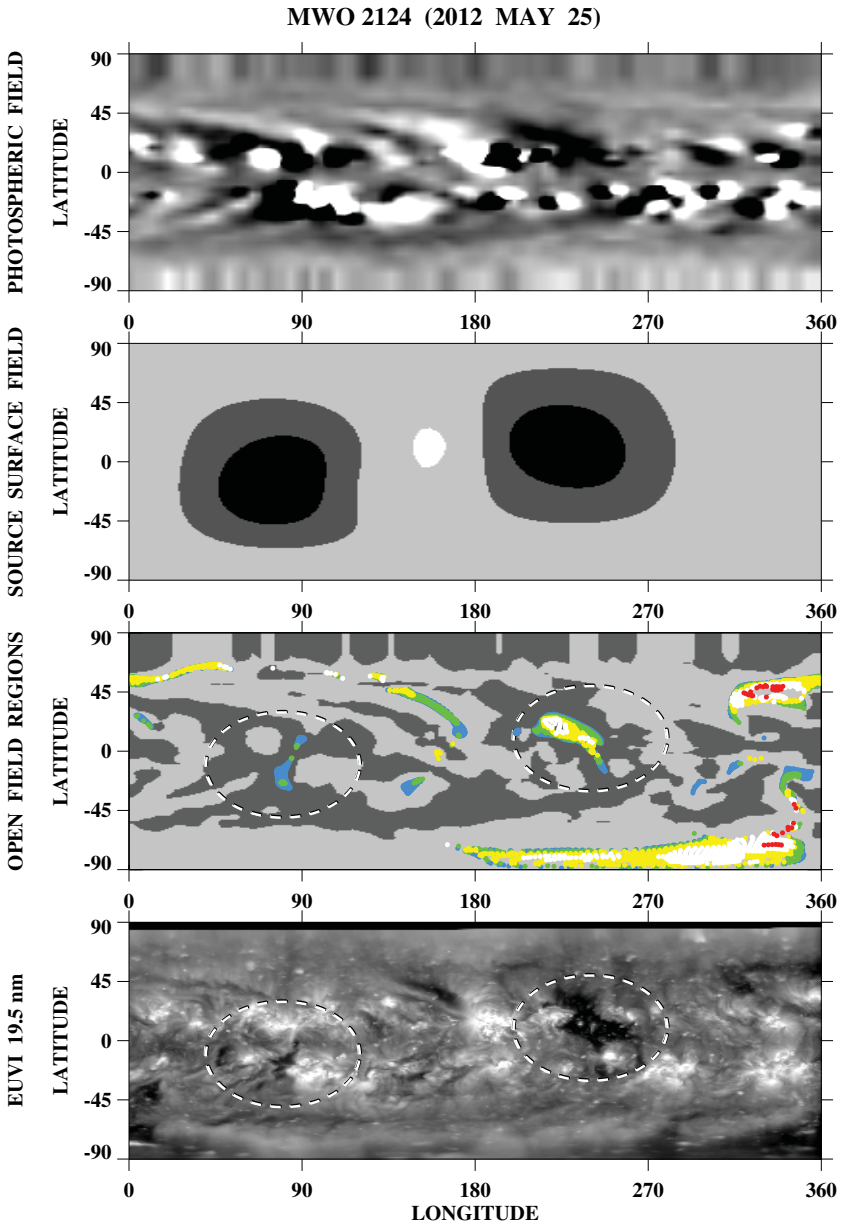

Figure 5. Latitude–longitude maps showing the large-scale field and distribution of coronal holes during CR 2124 (gray scale and color-coding as in Figure 2). Top panel: MWO photospheric field. Second panel: source-surface field $B_{ss} = B_r(R_{ss}, L, \phi)$. Third panel: PFSS-derived coronal holes. Bottom panel: distribution of Fe XII 19.5 nm emission recorded by *STEREO*/EUVI B between May 16 and June 12. In the bottom two maps, dashed circles identify the negative-polarity coronal holes on which the two cylindrical current sheets are centered.

(A color version of this figure is available in the online journal.)

pole, the overlying open field lines have positive polarity; this positive-polarity flux converges above the solar surface to form the high-latitude pseudostreamer plasma sheet seen in the top right panel of Figure 4 (compare the discussion of "polar streamers" during the cycle 23 maximum by Zhukov et al. 2008).

5. INTERPLANETARY SECTOR STRUCTURE AND SOLAR WIND SPEED

The assumption that the HCS extends radially outward from the source-surface neutral line allows us to derive the sector structure of the interplanetary magnetic field (IMF) in the ecliptic; comparison with in situ spacecraft measurements then provides a further check on the model. It is also interesting to compare the solar wind speed measured at Earth with that predicted using the inverse correlation between wind speed and the coronal flux-tube expansion factor, defined as $f_{ss} = (R_\odot/R_{ss})^2|B_0/B_{ss}|$, where B_0 denotes the footpoint field strength (see, e.g., Wang & Sheeley 1990; Arge & Pizzo 2000; Poduval & Zhao 2004).

The stackplots in Figure 8 display the observed IMF polarities and wind speeds near Earth from 2010 June to 2013 January (CR 2098–2132), along with the corresponding PFSS-based predictions. Here, each row of pixels represents a 27.3 day CR, with time running from right to left. Both the observed and predicted IMF polarities exhibit a four-sector structure during 2012, in contrast to the two-sector structure prevalent until late 2011. This behavior is consistent with Figure 6(b), which shows the dipole dominating over the quadrupole in 2011, but the opposite occurring in 2012. In the stackplots of

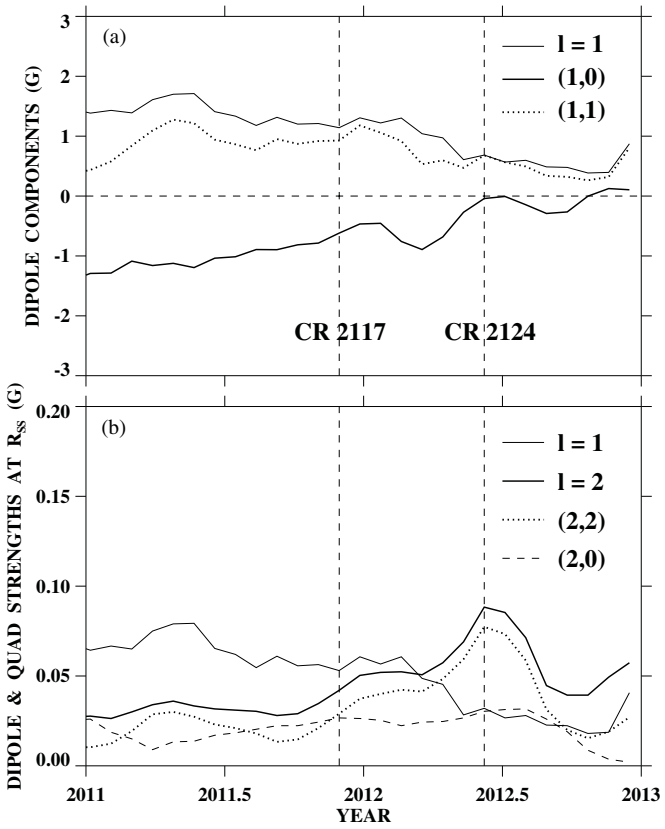

Figure 6. (a) Time variation of the total, axial, and equatorial dipole components of the MWO photospheric field during 2011–2012 (CR 2105–2132). The dipole strengths $D_{\rm tot}$ (thin solid line), $D_{\rm ax}$ (thick solid line), and $D_{\rm eq}$ (dotted) are expressed in Gauss, and three-rotation running means have been taken. The axial dipole component approaches zero in the middle of 2012. (b) Variation of the total dipole (thin solid line), total quadrupole (thick solid line), nonaxisymmetric (2, 2) quadrupole (dotted), and axisymmetric (2, 0) quadrupole (dashed) components of the source-surface field during 2011–2012. Again, MWO data have been used and three-rotation running means taken. The (2,2) quadrupole component provides the dominant contribution to the source-surface field in mid-2012. Magnetograph measurements from NSO/Kitt Peak and WSO yield similar curves.

wind speed, we see a strong recurrent high-speed stream during 2012, which emanates from the large low-latitude hole centered at $\phi \sim 240^\circ$ in the bottom two maps of Figure 5. A much weaker stream originates from the small hole near longitude 80°. Both streams are located inside negative-polarity sectors, and are thus confined within the two cylindrical current sheets.

6. SUMMARY AND DISCUSSION

Because of the rapid falloff of higher-order multipoles with height, the Sun's magnetic dipole component dominates at heliocentric distances $\gtrsim 2\,R_\odot$ through most of the sunspot cycle. As a result, the HCS normally has the form of a single structure (the "ballerina skirt"), which is warped by the presence of multipoles $l > 1$ and which is tilted by an angle that depends mainly on the ratio $D_{\rm eq}/D_{\rm ax}$. It is only during the relatively brief (~2 yr) period of polar field reversal that the total dipole moment may become sufficiently small for multiple current sheets to form. As $D_{\rm ax}$ approached zero in the middle of 2012, the Sun's nonaxisymmetric quadrupole component became so dominant that the HCS split into two cylindrical current sheets whose axes were centered approximately on the equator and separated by ~180° in longitude. The associated cylindrical plasma sheets gave rise to arclike features that could be identified

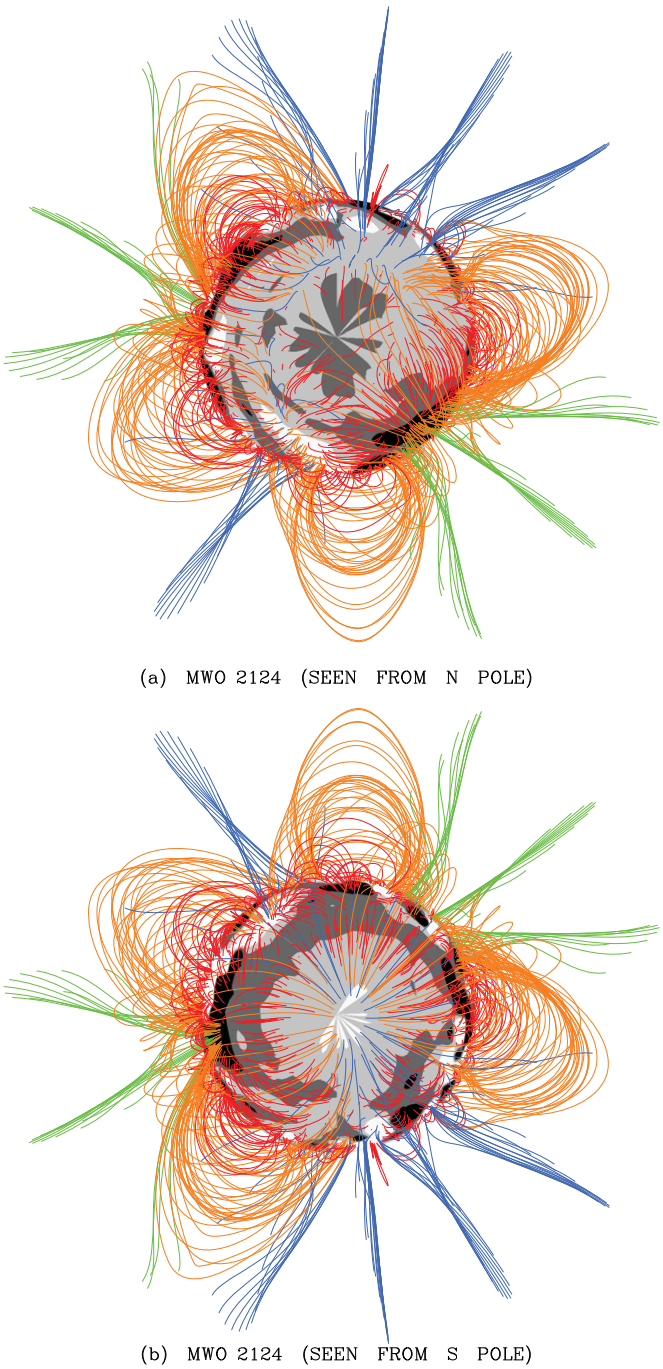

Figure 7. Coronal fieldline configuration during CR 2124, as viewed (a) from above the north pole, and (b) from above the south pole (PFSS extrapolation of MWO photospheric measurements). Closed loops are coded orange if they extend beyond $r = 1.5\,R_\odot$, red otherwise; open field lines are blue (green) if they have positive (negative) polarity. Black, dark gray, light gray, and white denote areas of the photosphere where $B_r < -6$ G, -6 G $< B_r < 0$ G, 0 G $< B_r <$ +6 G, and $B_r >$ +6 G, respectively. The coronal field is clearly dominated by the (2, 2) quadrupole component. Despite the residual negative-polarity photospheric flux at the north pole, the overlying open field lines have positive polarity, with a pseudostreamer located underneath.

(A color version of this figure is available in the online journal.)

in LASCO and SECCHI white-light maps. In addition, using EUV imaging data, we were able to locate the isolated negative-polarity coronal holes around which the cylindrical plasma/current sheets formed. To our knowledge, this case provides the best evidence so far for the multiple current sheets that have

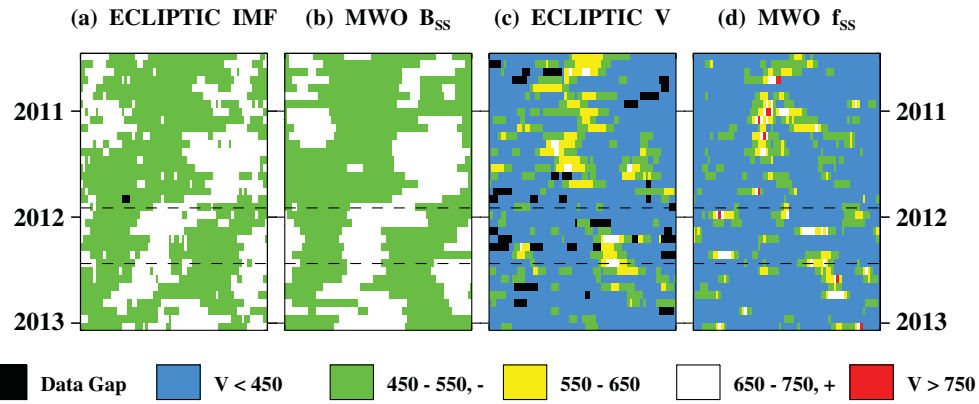

Figure 8. Variation of the IMF sector polarity and solar wind speed near Earth during 2010–2013, plotted in stackplot format, with each row of pixels representing a 27.3 day Carrington rotation and time running from right to left. (a) Polarity of the radial IMF component (white: positive/outward; green: negative/inward), as measured by the Magnetic Field Experiment on the *Advanced Composition Explorer* (MAG/*ACE*). (b) Polarities predicted from a PFSS extrapolation of MWO photospheric field measurements (CR 2098–2132). (c) Proton speeds measured by the Solar Wind Electron Proton Alpha Monitor (SWEPAM/*ACE*). (d) Wind speeds predicted using the inverse correlation between v and f_{ss} (color-coding as in Figure 2, third panel). A four-sector structure dominates during 2012. Horizontal dashed lines mark CR 2117 and CR 2124.

(A color version of this figure is available in the online journal.)

long been suggested by PFSS extrapolations of photospheric field measurements around sunspot maximum.

In closing, we emphasize the advantage of coronal streamer imaging over in situ spacecraft measurements in determining the global topology of the HCS. (See also Robbrecht & Wang 2012, where a similar procedure was used to measure the north–south displacement of the HCS, and compare the method of Erdős & Balogh 2010.) Because space- and Earth-based magnetometers can sample only one location at a time, such observations cannot distinguish between a single warped current sheet and two or more distinct structures. Although the method employed here is subject to the uncertainties inherent in the photospheric field data (which are noisy near the poles) and in the PFSS model, it exploits the ability of coronagraphs to image the entire streamer belt on timescales less than or on the order of a solar rotation; additional constraints and consistency checks are provided by EUV observations of the underlying coronal holes and by the timing of IMF sector crossings at Earth.

We are indebted to the referee for helpful comments, and to N. B. Rich, A. F. R. Thernisien, and L. Hutting for constructing the LASCO and SECCHI synoptic maps. This work was supported by NASA and the Office of Naval Research.

REFERENCES

Arge, C. N., & Pizzo, V. J. 2000, JGR, 105, 10465
Billings, D. E. 1966, A Guide to the Solar Corona (New York: Academic)
Erdős, G., & Balogh, A. 2010, JGR, 115, A01105
Hoeksema, J. T., Wilcox, J. M., & Scherrer, P. H. 1982, JGR, 87, 10331
Petrie, G. J. D., & Haislmaier, K. J. 2013, ApJ, 775, 100
Poduval, B., & Zhao, X. P. 2004, JGR, 109, A08102
Riley, P., Linker, J. A., & Mikić, Z. 2002, JGR, 107(A7), SSH 8-1
Robbrecht, E., & Wang, Y.-M. 2012, ApJ, 755, 135
Shiota, D., Tsuneta, S., Shimojo, M., et al. 2012, ApJ, 753, 157
Smith, E. J. 2001, JGR, 106, 15819
Svalgaard, L., & Kamide, Y. 2013, ApJ, 763, 23
Wang, Y.-M., Robbrecht, E., & Sheeley, N. R., Jr. 2009, ApJ, 707, 1372
Wang, Y.-M., & Sheeley, N. R., Jr. 1988, JGR, 93, 11227
Wang, Y.-M., & Sheeley, N. R., Jr. 1990, ApJ, 355, 726
Wang, Y.-M., & Sheeley, N. R., Jr. 1995, ApJL, 447, L143
Wang, Y.-M., Sheeley, N. R., Jr., & Rich, N. B. 2000, GeoRL, 27, 149
Wang, Y.-M., Sheeley, N. R., Jr., & Rich, N. B. 2007, ApJ, 658, 1340
Zhukov, A. N., Saez, F., Lamy, P., Llebaria, A., & Stenborg, G. 2008, ApJ, 680, 1532